Nanoscale

PAPER

View Article Online
View Journal | View Issue

Cite this: *Nanoscale*, 2022, **14**, 6518

Charge-induced proton penetration across two-dimensional clay materials†

Le Shi, *[a] Yushuan Gao,[a] Zhixuan Ying,[a] Ao Xu [b] and Yonghong Cheng[a]

Received 15th January 2022,
Accepted 1st April 2022

DOI: 10.1039/d2nr00262k

rsc.li/nanoscale

Two-dimensional clay materials possess superior thermal and chemical stability, and the intrinsic tubular channels in their atomic structure provide possible routes for proton penetration. Therefore, they are expected to overcome the lack of materials that can conduct protons between 100–500 °C. In this work, we investigated the detailed proton penetration mechanism across 2D clay nanosheets with different isomorphic substitutions and counterions using extensive *ab initio* molecular dynamics and metadynamics simulations. We found that the presence of negative surface charges can dramatically reduce the proton penetration energy barrier to about one-third that of the neutral case, making it a feasible choice for the design of next-generation high-temperature proton exchange membranes. By tuning the isomorphic substitutions, the proton conductivity of single-layer clay materials can be altered.

Introduction

Proton exchange membrane fuel cells (PEMFCs) are a promising energy conversion technology that can convert hydrogen energy into electricity. Their commercialization is currently hindered by the high price and scarcity of the platinum catalyst, which is likely to be poisoned by impurities such as CO during operation.[1–3] If the operating temperature of PEMFCs can be elevated to above 120 °C, the reaction kinetics will be greatly improved and the durability of the platinum catalyst will be extended. Moreover, non-expensive transition metal catalysts may replace the platinum catalyst to provide satisfactory performance, and the water/heat management systems will be greatly simplified. However, the development of high temperature PEMFCs (HT-PEMFCs) is impeded by the lack of suitable proton exchange membranes that can survive high temperatures above 120 °C.[4–6] Numerous efforts have been devoted to developing proton exchange membranes that can bear higher operating temperatures, such as polybenzimidazoles (PBIs)/functionalized PBIs doped with acid/ionic liquid,[7–9] Nafion composites with nanofillers such as titania nanotubes[10] or graphene oxide,[11] and sulfonated poly(ether sulfone) anchored with metal–organic frameworks.[12] Nevertheless, a proton exchange membrane material that can simultaneously provide satisfying proton conductivity as well as good chemical and mechanical stability at high temperatures is still urgently needed.

The emergence of two-dimensional (2D) materials has opened up a new avenue for the design of next-generation proton exchange membranes.[13] The proton conductivity across one-atom-thick crystals such as graphene, h-BN and graphyne have been investigated employing both theoretical[14–16] and experimental[17–19] approaches, and have demonstrated their potential to simultaneously provide satisfactory proton conductivity as well as high selectivity.

Smectite clays, such as mica and montmorillonite, consist of a 2D stack of inorganic layers made of an octahedral alumina sheet fused between two tetrahedral silica sheets. Isomorphic substitutions in the crystal structure, such as the substitution of Si by Al in tetrahedral sites or Al by Mg in octahedral sites, produce net negative surface charges, which are counter balanced by exchangeable interlayer cations such as K^+ and Li^+.[20,21] These clay materials can be exfoliated into 2D nanosheets *via* a simple ion exchange and ultrasonic procedure.[22] Due to their hydrophilic property as well as superior thermal and chemical stability, various kinds of clay nanoparticles have been added to proton conductive polymer matrixes to enhance their high-temperature performance.[23–25] When these clay materials are exfoliated into 2D nanosheets and then restacked into a thin film, protons can move along the interlayer galleries, resulting in high proton conductivity.[26,27]

In 2019, Mogg *et al.*[28] for the first time reported that monolayer clay materials can allow proton penetration across the 2D nanosheets through their intrinsic narrow tubular atomic channels with a relatively low energy barrier of about 0.2 eV, as shown in Fig. 1. They proposed that the proton penetration process can be facilitated by the hydroxyl functional groups

[a]*State Key Laboratory of Electrical Insulation and Power Equipment, Center of Nanomaterials for Renewable Energy, School of Electrical Engineering, Xi'an Jiaotong University, Xi'an 710049, China. E-mail: le.shi@mail.xjtu.edu.cn*
[b]*School of Aeronautics, Northwestern Polytechnical University, Xi'an 710072, China*
† Electronic supplementary information (ESI) available. See DOI: https://doi.org/10.1039/d2nr00262k

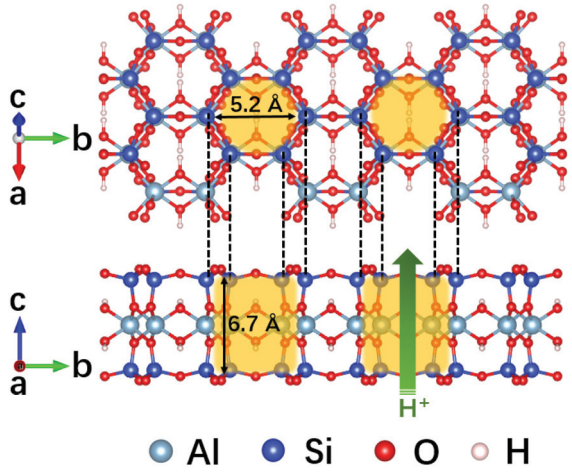

Fig. 1 Atomic geometry of a 2D clay nanosheet. Yellow shading highlights the tubular nanochannels in the atomic structure.

inside the tubular channels, resulting in a low energy barrier. Although previous work has suggested that hydroxyl functional groups can mediate proton transportation,[18,29] it is still surprising that protons can penetrate through such a long and narrow channel easily.

In this work, we systematically investigated the proton penetration behaviour across 2D clay nanosheets using extensive *ab initio* molecular dynamics (AIMD) and metadynamics simulations (>1 ns in total). We found that although the hydroxyl functional groups in the narrow tubular channel participate in the proton penetration process, it is the negative surface charges that are induced by the isomorphic substitution in clay materials that play a key role in increasing the cross-plane proton conductivity to an observable value. With negative surface charges on the 2D clay nanosheets, the water structure in the interfacial region and the proton distribution in the aqueous phase are significantly altered. Based on our metadynamics simulation results, the proton penetration energy barriers across the charged 2D clay nanosheets can be reduced to about one-third that in the neutral case. Considering the constraints applied during the metadynamics simulations and the neglected nuclear quantum effects, our calculation results show good consistency with experimental reports. We propose that by introducing negative surface charges on 2D clay nanosheets, their proton penetration energy barrier will be greatly reduced, making them a promising proton exchange membrane material that can operate in a high temperature range (100–500 °C).

Computational methodology

All the density functional theory (DFT) calculations were performed using the Abinit software package.[30–32] Perdew–Burke–Ernzerhof (PBE) generalized gradient approximation (GGA)[33] was employed as the exchange correlation functional. The projector-augmented-wave (PAW) method[34] was used to describe the electron–ion interaction. The cut-off energy was set at 20 Ha, and the *k*-point mesh was set to be <0.05 $Å^{-1}$. All the structures were fully optimized to a force tolerance of 5×10^{-4} Ha $Bohr^{-1}$.

MD simulations were carried out using the LAMMPS software package.[35,36] In the MD simulations, a ClayFF force field[37,38] was employed to characterize the interaction between the 2D clay nanosheets and aqueous environment. For all the MD simulations, the time step was set at 0.5 fs and a Nośe–Hoover chain thermostat[39] with a time constant of 0.1 ps was used to keep the temperature at T = 300 K. The pressure damping constant was set at 1 ps in the NPT simulations.

AIMD simulations were carried out using the CP2K software package.[40] *Ab initio* Born–Oppenheimer MD was used for the propagation of classical nuclei. The convergence criterion was set at 1×10^{-7} a.u. for the optimization of the wave function. Using the Gaussian and plane waves method, the wave function was expanded in the Gaussian double zeta with valence polarization function basis set (DZVP). An auxiliary basis set of plane waves was used to expand the electron density up to a cut-off of 400 Ry. The core electrons were treated using the PBE gradient[32] correction and Goedecker–Teter–Hutter (GTH) pseudopotentials.[41] Density functional theory (DFT)-D3 correction[42] was used to account for the van der Waals interaction. All the hydrogen atoms were replaced with deuterium atoms. For all the AIMD simulations, the time step was set at 0.5 fs, and a Nośe–Hoover chains thermostat with a time constant of 0.1 ps was employed to keep the temperature constant. As validated in our previous work, a temperature of around 400 K was necessary to obtain an oxygen–oxygen pair-correlation function comparable with that of the experiment at room temperature.[14,43–45] Therefore, for the AIMD simulations, the temperature was set at 400 K. It has been demonstrated that the AIMD simulation method employed in this work can characterize the proton hopping process in the aqueous environment accurately.[46,47]

The metadynamics simulations were performed using the CP2K software package[40] with the PLUMED plugin.[48] The deposition pace convergence test results are shown in Fig. S19, S25, S31, S37 and S43† and are listed in Table S2.† For each case, three metadynamics simulations with different initial geometries were performed, as listed in Table S3.† The width, height, and deposition frequency of the Gaussian "hills" employed in the production runs are listed in Table S4.†

Results and discussion

Water configuration around two-dimensional clay nanosheets

Proton exchange membranes usually operate in an aqueous (T < 100 °C) or highly humidified (T > 100 °C) environment. Under high-humidity conditions, water will condense on the clay surface and form a flat two-dimensional water film due to the high hydrophilicity of clay materials.[49,50] Recent experiments have demonstrated that the atomic structure of the interfacial hydration layers in a humidified environment is

identical to when the surfaces are immersed in the aqueous phase.[51] Therefore, we focus on the proton penetration behaviour that occurred in the 2D clay–water interface. The structure of exfoliated 2D pyrophyllite with a chemical formula of $Al_8Si_{16}O_{40}(OH)_8$ was optimized using DFT calculations and was adopted as the 2D neutral clay nanosheet (denoted as "Neutral"). Four charged systems were constructed based on this geometry, as shown in Fig. S1:† (1) substitution of four tetrahedral Si atoms by Al atoms together with four K^+ counterions for charge compensation (denoted as "Tetra&K^+"); (2) substitution of four tetrahedral Si atoms by Al atoms together with four Li^+ counterions for charge compensation (denoted as "Tetra&Li^+"); (3) substitution of four octahedral Al atoms with four Mg atoms together with four K^+ counterions for charge compensation (denoted as "Octa&K^+"); and (4) substitution of four octahedral Al atoms with four Mg atoms together with four Li^+ counterions for charge compensation (denoted as "Octa&Li^+"). These 2D clay nanosheets together with the counterions were put into a box filled with water with a density of 1 g cm^{-3}. Then, classical NPT MD simulations (P = 1 atm, T = 300 K) using the ClayFF force field[37,38] were performed for 2 ns with fixed x and y directions. Afterward, the systems were further equilibrated in an NVT ensemble (T = 300 K) for another 2 ns. Then, these equilibrated systems went through 20 ps AIMD simulations. The system configurations used for the AIMD simulations can be found in Table S1.†

We analysed the water density distribution and trajectories of counterions, as shown in Fig. 2b and Fig. S3–S11.† The water depletion region near the charged clay layer mainly comes from the size exclusion effect of charged ions. For tetrahedral substitutions, the counterions tend to attach on the clay nanosheets with an inner-sphere adsorption mode, while for the octahedral substitutions, some of the counterions will detach from the surface and exist in the aqueous phase, which is consistent with previous reports.[52] Water density profiles and trajectories of counterions calculated based on the last 500 ps NVT MD simulations are shown in Fig. S2,† which are similar to the AIMD simulations but exhibit smoother water density distribution due to the adequate sampling. The area occupied by the first layer of water molecules near the 2D clay nanosheets is classified as the interfacial ("IF") region, which is the 8 Å area surrounding the neutral slab and the 6 Å area surrounding the charged slabs. The other areas far away from the slabs are classified as the intermediate ("IM") region. Orientation distribution of water molecules in both the "IF" and "IM" regions was analysed and compared with the bulk water case, as shown in Fig. 3. It can be found that for all the considered systems, the "IM" water shows similar orientation distribution with that of bulk water, suggesting little influence of the nanosheets on the "IM" region. For the neutral case, the "IF" water orientation distribution is also consistent with the bulk water case. However, for charged 2D clay nanosheets, hydrogen atoms in the water molecules tend to point towards the clay surface. The presence of surface charges significantly alters the water density profiles and orientation distribution of water molecules neighbouring the 2D clay nanosheet.

Proton transportation near two-dimensional clay nanosheets

We studied the proton transportation behaviour near the neutral and charged 2D clay nanosheets by introducing an extra proton into the systems and connecting it with a random water molecule to form a hydronium ion. For the neutral case, the positive charge of the proton was compensated by a uniform background of negative charges. For the charged

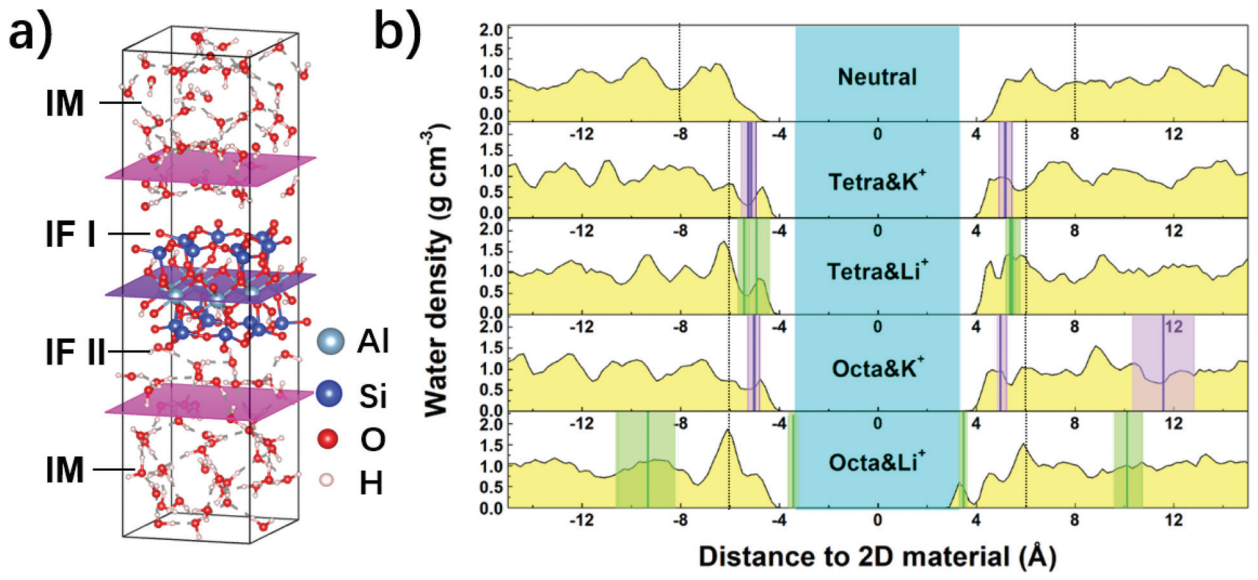

Fig. 2 (a) Setup for the AIMD simulation of the "Neutral" slab in the aqueous phase. (b) Density profiles of water as a function of distance to the 2D clay materials and the statistical positions of K^+ (purple line and shading) and Li^+ (green line and shading) calculated based on AIMD simulation trajectories. The cyan shading represents the position of the 2D clay nanosheets.

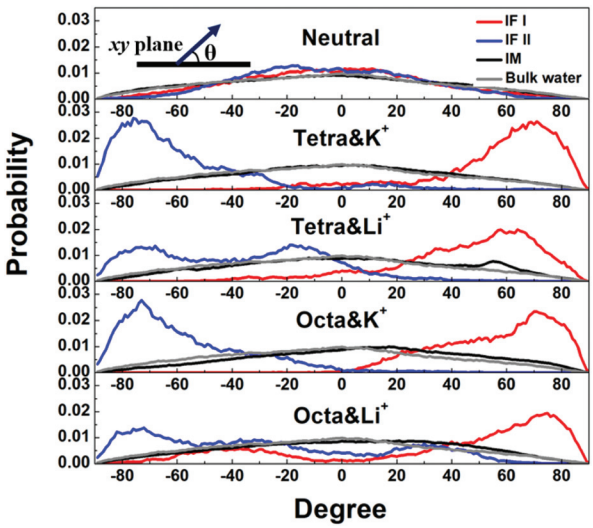

Fig. 3 Angle formed between the water dipole vector and the *xy*-plane. The data of "bulk water" was obtained from a 15 ps AIMD simulation of 64 water molecules in a cubic box with a water density of 1 g cm^{-3}.

cases, one of the counterions was removed to maintain system neutrality. For each system, 100 ps unbiased AIMD simulations in the NVT ensemble were performed. The trajectories of the proton and counterions can be found in Fig. S12–S14, S16 and S18.† It can be found that for the neutral system, the proton mainly exists in the "IM" region. However, for the charged systems, the proton will stay close to the 2D nanosheets and seems to be trapped in the "IF" region. The presence of protons did not significantly influence the movement of other counterions. We further calculated the free energy profiles of the proton as a function of distance to the 2D clay materials based on the following equation:[53]

$$F = -k_B T \ln(P_z) \quad (1)$$

where k_B is the Boltzmann constant, T = 300 K, and P_z is the probability that the proton appears in the distance of z to the 2D clay slab. As shown in Fig. 4a, the proton needs to overcome an energy barrier when approaching the neutral 2D clay nanosheets, which is consistent with the decreasing water density. For the charged clay systems as shown in Fig. 4b, S15, S17 and S19,† however, there exists an energy minimum of about 6 Å away from the centre of the 2D nanosheets, indicating that the proton prefers to transport among the first layer of water molecules near the 2D slab in these scenarios. The presence of negative surface charges effectively confined the movement of protons, which is similar to the OH^- transportation behaviour near the positively charged surface of 2D layered double hydroxide (LDH).[54–56]

Proton penetration across two-dimensional clay nanosheets

Throughout all the above unbiased AIMD simulations, the proton tends to exist in the aqueous phase and no spontaneous proton penetration behaviour across the 2D clay nanosheets can be observed. To evaluate the possibility of proton penetration, we performed *ab initio* metadynamics simulations to calculate the proton penetration across energy barriers. As the aqueous phases are separated by the 2D clay nanosheets, a proton has to dissociate from the hydronium ion when penetration occurs. To track the proton trajectories and deposit bias potentials, we constrained the O–H bonds of all the water molecules when the bond lengths exceed 1.4 nm to avoid the index change of the proton caused by Grotthuss migration. The distance between the proton and the 2D clay nanosheets was chosen as the collective variable. A pair of walls were put 8 Å away from the 2D neutral clay nanosheet and 6 Å away from the charged 2D clay nanosheets to confine the proton movement during the simulation, as shown in Fig. S20, S27, S34, S41 and S48.† The convergence of deposition pace for each case was tested using the same initial geometry, as shown in Fig. S21, S28, S35, S42 and S49† and listed in Table S2.† For each production run, three metadynamics simulations with different initial geometries were performed.

The proton trajectories during the metadynamics simulations and the detailed proton penetration energy barriers for

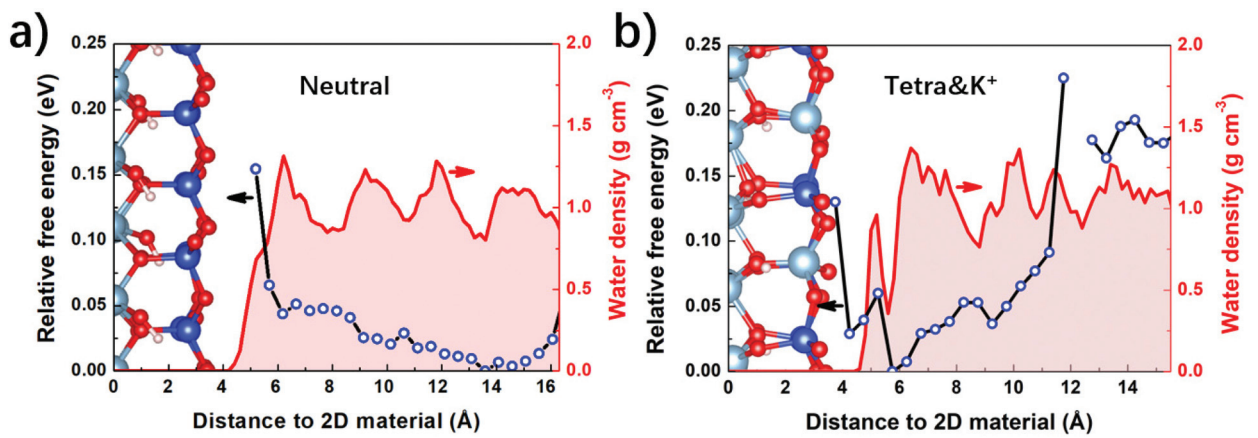

Fig. 4 Proton energy profile (black line with blue circles) and water density profile (red line with pink shading) as a function of distance to the 2D clay materials in (a) the "Neutral" system and (b) "Tetra&K^+" system.

each case are shown in Fig. S22–S24, S29–S31, S36–S38, S43–S45, and S50–S52† and are listed in Table S3.† For the neutral 2D clay nanosheet, the calculated proton penetration energy barrier is 2.02 ± 0.16 eV, as shown in Fig. 5a, which can barely occur at room temperature. For the charged 2D clay nanosheets, however, the calculated proton penetration energy barriers are dramatically decreased. The lowest energy barrier was observed for the "Tetra&K^+" case, as shown in Fig. 5b, where the energy barrier is 0.66 ± 0.10 eV, almost one-third that of the neutral 2D clay nanosheets. For the other cases, the energy barriers are 0.87 ± 0.15 eV ("Tetra&Li^+"), 0.74 ± 0.04 eV ("Octa&K^+") and 0.82 ± 0.13 eV ("Octa&Li^+"), all of which are much smaller than that of the neutral case. The detailed substitution sites and species of counterions show minor influence on the corresponding proton penetration energy barrier. As suggested in previous research, the proton penetration energy barrier can be about 0.5 eV lower when taking nuclear quantum effects into account.[57,58] Moreover, the constraints added during the metadynamics simulations may also result in a higher energy barrier. Therefore, the actual proton penetration energy barriers across the charged slabs should be lower than 0.3 eV, which is in good agreement with the experimental results reported by Mogg *et al.*[28]

For all the proton penetration energy profiles, the maximum energy value appears at the surface of the 2D clay nanosheets, which corresponds to the moment when the proton dissociates from the hydronium ion and begins to enter the tubular channel of the 2D clay structure. To clarify the detailed proton penetration mechanism, we monitored the O–H^+, Si–H^+, Al–H^+ and Mg–H^+ coordination numbers during the metadynamics simulations, as shown in Fig. S26, S33, S40, S47 and S54.† It can be found that for both the neutral and charged cases, the O–H^+ coordination number fluctuates around 1.0 during the entire simulation time, indicating that the proton always connects with an oxygen atom during the penetration process. The Si–H^+, Al–H^+ and Mg–H^+ coordination numbers always stay close to zero, suggesting little interaction between these atoms and the proton. These results reveal that the proton penetration behaviour across the 2D clay nanosheets are mediated by the surface oxygen atoms and hydroxyl functional groups in the 2D clay structure, which is consistent with the mechanism proposed by Mogg *et al.*[28] However, the proton penetration energy barrier of the neutral case indicates that the hydroxyl functional group alone is not enough to reduce the proton energy barrier to an acceptable value for proton exchange membranes. The thick atomic slab of 2D clay nanosheets can effectively block the penetration of any other species, which assures its selectivity when serving as a proton exchange membrane.

Conclusions

In this work, we systematically investigated the proton penetration behaviour across both neutral and charged 2D clay nanosheets using extensive AIMD and *ab initio* metadynamics simulations. Unlike the previously proposed theory, which states that the presence of hydroxyl functional groups inside the tubular channels of the 2D clay structure significantly reduces the proton penetration energy barrier,[28] we revealed that it is the surface charge that makes proton penetration across the long and narrow tubular channels possible to occur at room temperature. The surface charges can be introduced by isomorphic substitutions in both the tetrahedral Si site or the octahedral Al site, and can alter the neighbouring hydrogen bond network and confine protons within the first layer of neighbouring water molecules.

Compared with other 2D materials such as graphene, graphyne and h-BN, 2D clay nanosheets have evident advantages such as an abundance of precursors, superior chemical and thermal stability and easy exfoliation procedures. The thick atomic slab of the 2D clay nanosheets can effectively block the penetration of any other species, which assures its selectivity when serving as a proton exchange membrane. Our results

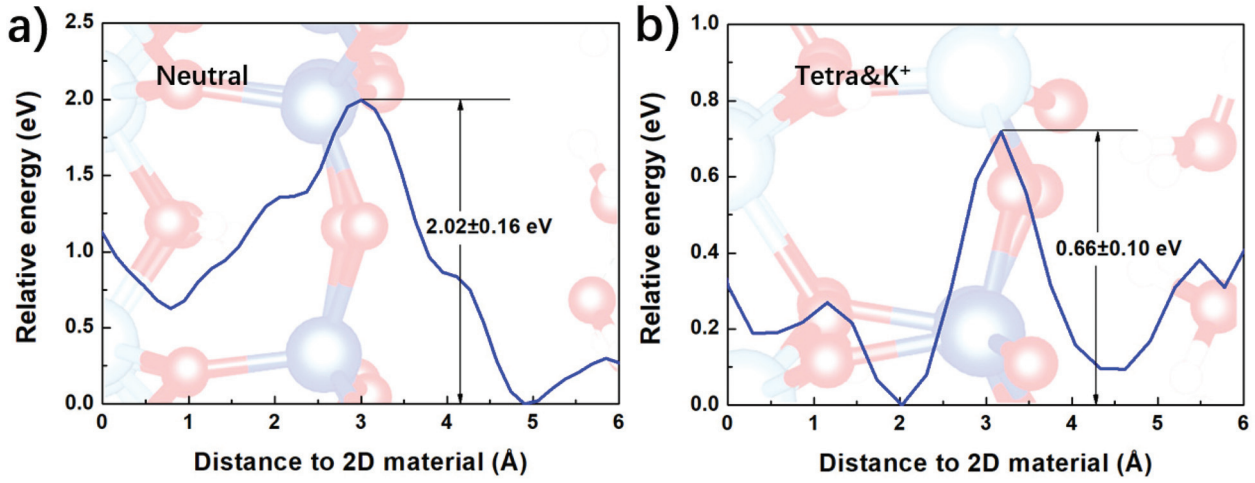

Fig. 5 Free energy profiles of proton penetration across 2D clay materials in (a) the "Neutral" system and (b) "Tetra&K^+" system.

show that with surface charges, the proton penetration energy barrier can be dramatically decreased to a value suitable for proton conduction. All these properties suggest that 2D clay materials are a prospective candidate for the design of next-generation proton exchange membranes for HT-PEMFCs.

Author contributions

L. S. conceived the research and designed the numerical simulations; L. S., Y. G., Z. Y. and A. X analysed the data; L. S. wrote the paper; L. S., Y. G., Z. Y., A. X. and Y. C discussed the manuscript.

Conflicts of interest

There are no conflicts to declare.

Acknowledgements

The work described in this paper was supported by the National Natural Science Foundation of China (51907159) and the Young Talent Recruiting Plans of Xi'an Jiaotong University (DQ6J002). The simulations were supported by HPC Platform, Xi'an Jiaotong University.

References

1 Y. Song, C. Zhang, C. Ling, M. Han, R. Yong, D. Sun and J. Chen, Review on current research of materials, fabrication and application for bipolar plate in proton exchange membrane fuel cell, *Int. J. Hydrogen Energy*, 2020, **45**, 29832–29847.

2 L. Xue, Y. Li, X. Liu, Q. Liu, J. Shang, H. Duan, L. Dai and J. Shui, Zigzag carbon as efficient and stable oxygen reduction electrocatalyst for proton exchange membrane fuel cells, *Nat. Commun.*, 2018, **9**, 1–8.

3 A. Kongkanand and M. Mathias, The priority and challenge of high-power performance of low-platinum proton-exchange membrane fuel cells, *J. Phys. Chem. Lett.*, 2016, **7**, 1127–1137.

4 Q. Li, J. Jensen, R. Savinell and N. Bjerrum, High temperature proton exchange membranes based on polyben-zimidazoles for fuel cells, *Prog. Polym. Sci.*, 2009, **34**, 449–477.

5 R. Rosli, A. Sulong, W. Daud, M. Zulkifley, T. Hu-saini, M. Rosli, E. Majlan and M. Haque, A review of high-temperature proton exchange membrane fuel cell (HT-PEMFC) system, *Int. J. Hydrogen Energy*, 2017, **42**, 92293–99314.

6 R. Haider, Y. Wen, Z. Ma, D. Wilkinson, L. Zhang, X. Yuan, S. Song and J. Zhang, High temperature proton exchange membrane fuel cells: progress in advanced materials and key technologies, *Chem. Soc. Rev.*, 2021, **50**, 1138–1187.

7 S. Bhadra, N. Kim and J. Lee, A new self-cross-linked, net-structured, proton conducting polymer membrane for high temperature proton exchange membrane fuel cells, *J. Membr. Sci.*, 2010, **349**, 304–311.

8 M. Haque, A. Sulong, K. Loh, E. Majlan, T. Husaini and R. Rosli, Acid doped polybenzimidazoles based membrane electrode assembly for high temperature proton exchange membrane fuel cell: A review, *Int. J. Hydrogen Energy*, 2017, **42**, 9156–9179.

9 E. van de Ven, A. Chairuna, G. Merle, S. Benito, Z. Borneman and K. Nijmeijer, Ionic liquid doped polybenzimidazole membranes for high temperature Proton Exchange Membrane fuel cell applications, *J. Power Sources*, 2013, **222**, 202–209.

10 Y. Jun, H. Zarrin, M. Fowler and Z. Chen, Functionalized titania nanotube composite membranes for high temperature proton exchange membrane fuel cells, *Int. J. Hydrogen Energy*, 2011, **36**, 6073–6081.

11 H. Zarrin, D. Higgins, Y. Jun, Z. Chen and M. Fowler, Functionalized graphene oxide nanocomposite membrane for low humidity and high temperature proton exchange membrane fuel cells, *J. Phys. Chem. C*, 2011, **115**, 20774–20781.

12 N. Anahidzade, A. Abdolmaleki, M. Dinari, K. Tadavani and M. Zhiani, Metal-organic framework anchored sulfonated poly (ether sulfone) as a high temperature proton exchange membrane for fuel cells, *J. Membr. Sci.*, 2018, **565**, 281–292.

13 G. Liu, W. Jin and N. Xu, Two-dimensional-material membranes: a new family of high-performance separation membranes, *Angew. Chem., Int. Ed.*, 2016, **55**, 13384–13397.

14 L. Shi, A. Xu, D. Pan and T. Zhao, Aqueous proton-selective conduction across two-dimensional graphyne, *Nat. Commun.*, 2019, **10**, 1–8.

15 J. Xu, H. Jiang, Y. Shen, X. Li, E. Wang and S. Meng, Transparent proton transport through a two-dimensional nanomesh material, *Nat. Commun.*, 2019, **10**, 1–8.

16 L. Shi, A. Xu, G. Chen and T. Zhao, Theoretical understanding of mechanisms of proton exchange membranes made of 2D crystals with ultrahigh selectivity, *J. Phys. Chem. Lett.*, 2017, **8**, 4354–4361.

17 S. Hu, M. Lozada-Hidalgo, F. Wang, A. Mishchenko, F. Schedin, R. Nair, E. Hill, D. Boukhvalov, M. Katsnelson, R. Dryfe and I. Grigorieva, Proton transport through one-atom-thick crystals, *Nature*, 2014, **516**, 227–230.

18 J. Achtyl, R. Unocic, L. Xu, Y. Cai, M. Raju, W. Zhang, R. Sacci, I. Vlassiouk, P. Fulvio, P. Ganesh and D. Wesolowski, Aqueous proton transfer across single-layer graphene, *Nat. Commun.*, 2015, **6**, 1–7.

19 J. Liu, L. Yu, X. Cai, U. Khan, Z. Cai, J. Xi, B. Liu and F. Kang, Sandwiching h-BN monolayer films between sulfonated poly (ether ether ketone) and Nafion for proton exchange membranes with improved ion selectivity, *ACS Nano*, 2019, **13**, 2094–2102.

20 B. Rotenberg, V. Marry, R. Vuilleumier, N. Malikova, C. Simon and P. Turq, Water and ions in clays: Unraveling the interlayer/micropore exchange using molecular dynamics, *Geochim. Cosmochim. Acta*, 2007, **71**, 5089–5101.

21 I. Akita, Y. Ishida and T. Yonezawa, Atomic-scale imaging of a free-standing monolayer clay mineral nanosheet using scanning transmission electron microscopy, *J. Phys. Chem. Lett.*, 2020, **11**, 3357–3361.
22 V. Nicolosi, M. Chhowalla, M. Kanatzidis, M. Strano and J. Coleman, Liquid exfoliation of layered materials, *Science*, 2013, **340**, 6139.
23 J. Arias, J. Dutra and A. de Souza Gomes, Hybrid membranes of sulfonated poly ether ether ketone, ionic liquid and organically modified montmorillonite for proton exchange membranes with enhanced ionic conductivity and ionic liquid lixiviation protection, *J. Membr. Sci.*, 2017, **537**, 353–361.
24 M. Hasani-Sadrabadi, E. Dashtimoghadam, F. Majedi, K. Kabiri, M. Solati-Hashjin and H. Moaddel, Novel nanocomposite proton exchange membranes based on Nafion® and AMPS-modified montmorillonite for fuel cell applications, *J. Membr. Sci.*, 2010, **365**, 286–293.
25 Y. Huang, Y. Ye, Y. Syu, B. Hwang and F. Chang, Synthesis and characterization of sulfonated polytriazole-clay proton exchange membrane by in situ polymerization and click reaction for direct methanol fuel cells, *J. Power Sources*, 2012, **208**, 144–152.
26 L. Cao, H. Wu, X. He, H. Geng, R. Zhang, M. Qiu, P. Yang, B. Shi, N. Khan and Z. Jiang, Flexible, transparent ion-conducting membranes from two-dimensional nanoclays of intrinsic conductivity, *J. Mater. Chem. A*, 2019, **7**, 25657–25664.
27 J. Shao, K. Raidongia, A. Koltonow and J. Huang, Self-assembled two-dimensional nanofluidic proton channels with high thermal stability, *Nat. Commun.*, 2015, **6**, 1–7.
28 L. Mogg, G. Hao, S. Zhang, C. Bacaksiz, Y. Zou, S. Haigh, F. Peeters, A. Geim and M. Lozada-Hidalgo, Atomically thin micas as proton-conducting membranes, *Nat. Nanotechnol.*, 2019, **14**, 962–966.
29 L. Shi, Z. Ying, A. Xu and Y. Cheng, Unraveling the water-mediated proton conduction mechanism along the surface of graphene oxide, *Chem. Mater.*, 2020, **32**, 6062–6069.
30 X. Gonze, J. Beuken, R. Caracas, F. Detraux, M. Fuchs, G. Rignanese, L. Sindic, M. Verstraete, G. Zerah, F. Jollet and M. Torrent, First-principles computation of material properties: the ABINIT software project, *Comput. Mater. Sci.*, 2002, **25**, 478–492.
31 X. Gonze, B. Amadon, P. Anglade, J. Beuken, F. Bottin, P. Boulanger, F. Bruneval, D. Caliste, R. Caracas, M. Côté and T. Deutsch, ABINIT: first-principles approach to material and nanosystem properties, *Comput. Phys. Commun.*, 2009, **180**, 2582–2615.
32 X. Gonze, A brief introduction to the ABINIT software package, *Z. Kristallogr. – Cryst. Mater.*, 2005, **220**, 558–562.
33 J. Perdew, M. Ernzerhof and K. Burke, Rationale for mixing exact exchange with density functional approximations, *J. Chem. Phys.*, 1996, **105**, 9982–9985.
34 P. Blöchl, Projector augmented-wave method, *Phys. Rev. B: Condens. Matter Mater. Phys.*, 1994, **50**, 17953.
35 S. Plimpton, Fast Parallel Algorithms for Short-Range Molecular Dynamics, *J. Comput. Phys.*, 1995, **117**, 1–19.
36 H. Aktulga, J. Fogarty, S. Pandit and A. Grama, Parallel Reactive Molecular Dynamics: Numerical Methods and Algorithmic Techniques, *Parallel Comput.*, 2012, **38**, 245–259.
37 R. Cygan, J. Liang and A. Kalinichev, Molecular models of hydroxide, oxyhydroxide, and clay phases and the development of a general force field, *J. Phys. Chem. B*, 2004, **108**, 1255–1266.
38 R. Cygan, J. Greathouse, H. Heinz and A. Kalinichev, Molecular models and simulations of layered materials, *J. Mater. Chem.*, 2009, **19**, 2470–2481.
39 G. Martyna, M. Klein and M. Tuckerman, Nosé-Hoover chains: the canonical ensemble via continuous dynamics, *J. Chem. Phys.*, 1992, **97**, 2635–2643.
40 J. VandeVondele, M. Krack, F. Mohamed, M. Parrinello, T. Chassaing and J. Hutter, Quickstep: Fast and accurate density functional calculations using a mixed Gaussian and plane waves approach, *Comput. Phys. Commun.*, 2005, **167**, 103–128.
41 S. Goedecker, M. Teter and J. Hutter, Separable dual-space Gaussian pseudopotentials, *Phys. Rev. B: Condens. Matter Mater. Phys.*, 1996, **54**, 1703.
42 S. Grimme, J. Antony, S. Ehrlich and H. Krieg, A consistent and accurate ab initio parametrization of density functional dispersion correction (DFT-D) for the 94 elements H-Pu, *J. Chem. Phys.*, 2010, **132**, 154104.
43 T. Pham, T. Ogitsu, E. Lau and E. Schwegler, Structure and dynamics of aqueous solutions from PBE-based first-principles molecular dynamics simulations, *J. Chem. Phys.*, 2016, **145**, 154501.
44 J. VandeVondele, F. Mohamed, M. Krack, J. Hutter, M. Sprik and M. Parrinello, The influence of temperature and density functional models in ab initio molecular dynamics simulation of liquid water, *J. Chem. Phys.*, 2005, **122**, 014515.
45 K. Brorsen, S. Willow, S. Xantheas and M. Gordon, The melting temperature of liquid water with the effective fragment potential, *J. Phys. Chem. Lett.*, 2015, **6**, 3555–3559.
46 G. F. Mangiatordi, E. Bremond and C. Adamo, DFT and, proton transfer reactions: a benchmark study on structure and kinetics, *J. Chem. Theory Comput.*, 2012, **8**, 3082–3088.
47 A. Hassanali, F. Giberti, J. Cuny, T. D. Kühne and M. Parrinello, Proton, transfer through the water gossamer, *Proc. Natl. Acad. Sci. U. S. A.*, 2013, **110**, 13723–13728.
48 M. Bonomi, D. Branduardi, G. Bussi, C. Camilloni, D. Provasi, P. Raiteri, D. Donadio, F. Marinelli, F. Pietrucci, R. Broglia and M. Parrinello, PLUMED: a portable plugin for free-energy calculations with molecular dynamics, *Comput. Phys. Commun.*, 2009, **180**, 1961–1972.
49 L. Xu, A. Lio, J. Hu, D. Ogletree and M. Salmeron, Wetting and capillary phenomena of water on mica, *J. Phys. Chem. B*, 1998, **102**, 540–548.
50 W. Cantrell and G. Ewing, Thin film water on muscovite mica, *J. Phys. Chem. B*, 2001, **105**, 5434–5439.

51 M. Uhlig and R. Garcia, In situ atomic-scale imaging of inter-facial water under 3D nanoscale confinement, *Nano Lett.*, 2021, **13**, 5593–5598.
52 P. Mignon, P. Ugliengo, M. Sodupe and E. Hernandez, Ab initio molecular dynamics study of the hydration of Li^+, Na^+ and K^+ in a montmorillonite model. Influence of isomorphic substitution, *Phys. Chem. Chem. Phys.*, 2010, **12**, 688–697.
53 D. Munoz-Santiburcio and D. Marx, On the complex structural diffusion of proton holes in nanoconfined alkaline solutions within slit pores, *Nat. Commun.*, 2016, **7**, 1–9.
54 L. Shi, Z. Ying, A. Xu and Y. Cheng, Unraveling the hydroxide ion transportation mechanism along the surface of two-dimensional layered double hydroxide nanosheets, *J. Phys. Chem. C*, 2021, **125**, 1240–1248.
55 P. Sun, R. Ma, X. Bai, K. Wang, H. Zhu and T. Sasaki, Single-layer nanosheets with exceptionally high and anisotropic hydroxyl ion conductivity, *Sci. Adv.*, 2017, **3**, e1602629.
56 P. Sun, F. Chen, W. Zhou, X. Liu, R. Ma and T. Sasaki, Superionic conduction along ordered hydroxyl networks in molecular-thin nanosheets, *Mater. Horiz.*, 2019, **6**, 2087–2093.
57 I. Poltavsky, L. Zheng, M. Mortazavi and A. Tkatchenko, Quantum tunneling of thermal protons through pristine graphene, *J. Chem. Phys.*, 2018, **148**, 204707.
58 Y. Feng, J. Chen, W. Fang, E. Wang, A. Michaelides and X. Li, Hydrogenation facilitates proton transfer through two-dimensional honeycomb crystals, *J. Phys. Chem. Lett.*, 2017, **8**, 6009–6014.